RESEARCH ARTICLE

NANO · MICRO small
www.small-journal.com

Highly Active CoNi-CoN_3 Composite Sites Synergistically Accelerate Oxygen Electrode Reactions in Rechargeable Zinc–Air Batteries

Nan Li, Mingzi Sun, Jiaxiang Xiao, Xiaoyu Ma, Lijuan Huang, Hongyu Li, Chao Xie, Yahui Yang, Hao Jiang,* Bolong Huang,* and Wenjun Zhang**

Reaching rapid reaction kinetics of oxygen reduction (ORR) and oxygen evolution reactions (OER) is critical for realizing efficient rechargeable zinc–air batteries (ZABs). Herein, a novel CoNi-CoN_3 composite site containing CoNi alloyed nanoparticles and CoN_3 moieties is first constructed in N-doped carbon nanosheet matrix (CoNi-CoN_3/C). Benefiting from the high electroactivity of CoNi-CoN_3 composite sites and large surface area, CoNi-CoN_3/C shows a superior half-wave potential (0.88 V versus RHE) for ORR and a small overpotential (360 mV) for OER at 10 mA cm^{-2}. Theoretical calculations have demonstrated that the introduction of CoNi alloys has modulated the electronic distributions near the CoN_3 moiety, inducing the d-band center of CoNi-CoN_3 composite site to shift down, thus stabilizing the valence state of Co active sites and balancing the adsorption of OER/ORR intermediates. Accordingly, the reaction energy trends exhibit optimized overpotentials for OER/ORR, leading to superior battery performances. For aqueous and flexible quasi-solid-state rechargeable ZABs with CoNi-CoN_3/C as catalyst, a large power density (250 mW cm^{-2}) and high specific capacity (804 mAh g^{-1}) are achieved. The in-depth understanding of the electroactivity enhancement mechanism of interactive metal nanoparticles and metal coordinated with nitrogen (MN_x) moieties is crucial for designing novel high-performance metal/nitrogen-doped carbon (M—N—C) catalysts.

1. Introduction

Rechargeable zinc–air batteries (ZABs) have attracted widespread interest due to their merits of high theoretical energy density, extraordinary safety, and low cost.[1–3] In ZABs, oxygen reduction (ORR) and oxygen evolution reactions (OER) are two key reactions that occur at the oxygen electrode during discharging and charging processes, respectively;[4,5] and the performance of rechargeable ZABs is strongly determined by the kinetics of these oxygen electrode reactions.[6–8] Thus far, noble metal-based materials (such as Pt and Ir) were considered as efficient catalysts for accelerating ORR or OER processes.[9–11] Nevertheless, the scarcity, high cost, and single functionality of these noble metal-based catalysts hinder their practical applications.[12–15] Therefore, the design and development of low-cost non-noble metal-based catalysts with excellent catalytic activity and cycling stability are essential for updating ZAB technology.

Due to their high intrinsic catalytic activity, high atom utilization efficiency and low cost, transition metal single atoms anchored on nitrogen-doped carbon (M—N—C, M = Fe, Co, Ni, etc.) have demonstrated their strong capabilities as bifunctional catalysts for oxygen electrode reactions.[16–19] In these catalysts, metal coordinated with nitrogen (MN_x) (x = 1–6) moieties have been elucidated to be predominant active sites.[17,18] Generally, the MN_x moieties with different coordination numbers endow the single atomic

N. Li, J. Xiao, X. Ma, L. Huang, H. Li, C. Xie, Y. Yang, H. Jiang
College of Chemistry and Chemical Engineering
Hunan Normal University
Changsha 410081, China
E-mail: yangyahui@hunnu.edu.cn; jianghao@hunnu.edu.cn

The ORCID identification number(s) for the author(s) of this article can be found under https://doi.org/10.1002/smll.202401506

DOI: 10.1002/smll.202401506

M. Sun, B. Huang
Department of Applied Biology and Chemical Technology
The Hong Kong Polytechnic University
Hung Hom, Kowloon, Hong Kong SAR 999077, China
E-mail: bhuang@polyu.edu.hk

H. Jiang, W. Zhang
Department of Materials Science and Engineering
& Center of Super-Diamond and Advanced Films
City University of Hong Kong
83 Tat Chee Avenue, Kowloon, Hong Kong SAR 999077, China
E-mail: apwjzh@cityu.edu.hk

M—N—C with diverse ORR/OER electrocatalytic activity and selectivity.[20–22] For example, recent studies have shown that CoN_3 site, with an asymmetric planar structure, is more favorable for a four-electron ORR process compared to the CoN_4 site.[22–24] However, the performance of single atomic MN_x catalysts still faces challenges due to the imbalanced adsorption/desorption strength of oxygen-containing intermediates on the MN_x site surface and the potential risk of oxidation degradation for MN_x site at high OER potentials. Consequently, achieving an overall performance that surpasses that of precious metal-based catalysts remains difficult for single atomic MNx catalysts.

Constructing composite site to regulate the local chemical environment and electronic structure around MN_x moieties has shown promise in optimizing the adsorption/desorption behavior of oxygen-containing intermediates on the catalyst surface and potentially improving the catalytic activity and stability of MN_x moieties.[25–27] Recent studies have also highlighted the ability of the metal or metal alloyed nanoparticles (M-NPs) in M—N—C materials to adjust the electronic distribution of the single atomic MN_4 moieties and promote ORR reactivity.[28–30] For instance, Sun et al. discovered that the coexistent FeCo NPs increased the local charge density of FeN_4 moieties, leading to enhanced O_2 adsorption, elongated O—O bond lengths, and facilitated cleavage of the O—O bond.[31] While there have been relevant studies exploring the interaction between M-NPs (*e.g.*, single elemental or alloyed) and single atomic MN_4 moieties, it remains unclear whether the nature of M-NPs and the coordination of MN_3 moieties can affect the electronic structure of M—N—C catalysts and their electrocatalytic activity towards ORR/OER.

In this work, a new type of CoNi-CoN_3 composite site containing CoNi alloyed NPs and three-coordinated CoN_3 moieties was constructed in ultrathin N-doped porous carbon nanosheet matrix (CoNi-CoN_3/C). The as-prepared CoNi-CoN_3/C exhibits superior ORR/OER bifunctional activity and stability in the alkaline electrolyte. Density-functional theory (DFT) calculations demonstrate that the electronic modulation induced by the introduction of neighboring CoNi alloys not only optimizes the electronic distribution of the CoN_3 active site, but also downregulates the position of the d-band center of the CoNi-CoN_3 composite site. Therefore, the adsorption/desorption free energy of the O-containing intermediates is moderated, and the overpotential of the rate-determining step is reduced, ensuring efficient ORR and OER. Significantly, the aqueous rechargeable ZABs based on CoNi-CoN_3/C oxygen electrodes deliver a power density of 250 mW cm^{-2} and maintain a small voltage gap of 0.94 V even after 2850 cycles (≈950 h). Moreover, a high specific capacity of over 800 mAh g^{-1} and remarkable flexibility are also achieved for CoNi-CoN_3/C based quasi-solid-state ZABs, demonstrating their great potential as power sources for wearable devices.

2. Results and Discussion

2.1. Synthesis and Characterization of CoNi-CoN_3/C

Figure 1a illustrates schematically the synthesis processes of CoNi-CoN_3/C. First, 2D NiZn bimetallic zeolitic imidazolate framework (NiZn-ZIF) nanosheets were synthesized by a wet-chemistry method. Co^{2+} was then introduced and competitively coordinated with the organic ligand of NiZn-ZIF, resulting in the self-splitting of NiZn-ZIF nanosheets and the formation of NiZn-ZIF-Co^{2+} composite with rich low-coordination edges. During the subsequent high-temperature pyrolysis of NiZn-ZIF-Co^{2+}, the inner Ni atoms and the outer Co atoms migrated to the intermediate carbon layer through the channels created due to the volatilization of Zn atoms. Finally, CoNi-CoN_3 composite sites (CoNi-CoN_3/C) were obtained through the alloying of Co/Ni atoms and the coordination of Co/N atoms with N dopants in carbon nanosheets. To comparatively study the effects of alloying on the electrocatalytic activity, single metallic Co—N/C and Ni—N/C samples were also prepared (Figure S1, Supporting Information).

As revealed by scanning electron microscopy (SEM) observations, in comparison with NiZn-ZIF (Figure 1b,c) and NiZn-ZIF-Co^{2+} precursors (Figure 1d,e), the CoNi-CoN_3/C nanosheets have rougher surfaces with much reduced lateral size (Figure 1f,g). The atomic force microscopy (AFM) profiles verify that the average thickness of CoNi-CoN_3/C nanosheets is ≈2.8 nm (Figure 1h,i). The 2D ultrathin nanosheet structure of CoNi-CoN_3/C is beneficial for exposing more catalytic sites and shortening the electron transport path during the electrocatalytic process. The transmission electron microscopy (TEM) image in **Figure 2a** further shows that, in CoNi-CoN_3/C, a large number of metal NPs are embedded in N-doped porous carbon nanosheets. Close observations by high-resolution TEM images (Figure 2b,c) demonstrate that the metal NPs are surrounded by multi-layered graphite carbon shells, which can effectively prevent the corrosion and leaching of active substances during electrocatalysis.[8,32] The distinct lattice fringes with *d*-spacings of 0.18 and 0.26 nm can be clearly observed in the high-resolution TEM image (insets in Figure 2c), which are assigned to the (200) and (111) planes of CoNi alloy (Figure S2, Supporting Information), respectively.[33] Additionally, the scanning TEM (STEM) and the spatially-resolved energy dispersive spectroscopy (EDS) elemental mapping images (Figure 2d–i) reveal uniform distributions of C and N in nanosheets. The O species in the CoNi-CoN_3/C sample are derived from the surface oxidation of metal particles in the air. In particular, the highly overlapped Co and Ni signals in the element mapping images also demonstrate the alloyed nature of Co–Ni NPs in CoNi-CoN_3/C. The contents of Co and Ni elements in CoNi-CoN_3/C are 3.35 and 0.23 wt%, respectively, as measured by inductively coupled plasma optical emission spectroscopy (ICP-OES).

The pore structure and specific surface area of CoNi-CoN_3/C were investigated by nitrogen adsorption–desorption tests.[34] A typical type IV isotherm with an obvious hysteresis loop in the relative high-pressure range (P/P_0 = 0.8–1.0) and dramatic increasing adsorption in the relative low-pressure range (P/P_0 = 0–0.015) are detected (Figure S3a, Supporting Information), suggesting a hierarchical micro/mesoporous structure of CoNi-CoN_3/C.[35] In comparison with the control samples of Co—N/C (543.1 m^2 g^{-1}) and Ni—N/C (79.4 m^2 g^{-1}), CoNi-CoN_3/C possesses the largest specific surface area of 744.5 m^2 g^{-1}. The pore size distribution curve further confirms the hierarchical micro/mesoporous structure of CoNi-CoN_3/C (Figure S3b, Supporting Information). Overall, the high surface area and hierarchical micro/mesoporous structure of CoNi-CoN_3/C are conducive to exposing more CoNi-CoN_3 composite sites and accelerating the charge/mass transfer during the electrocatalytic process.[35–38]

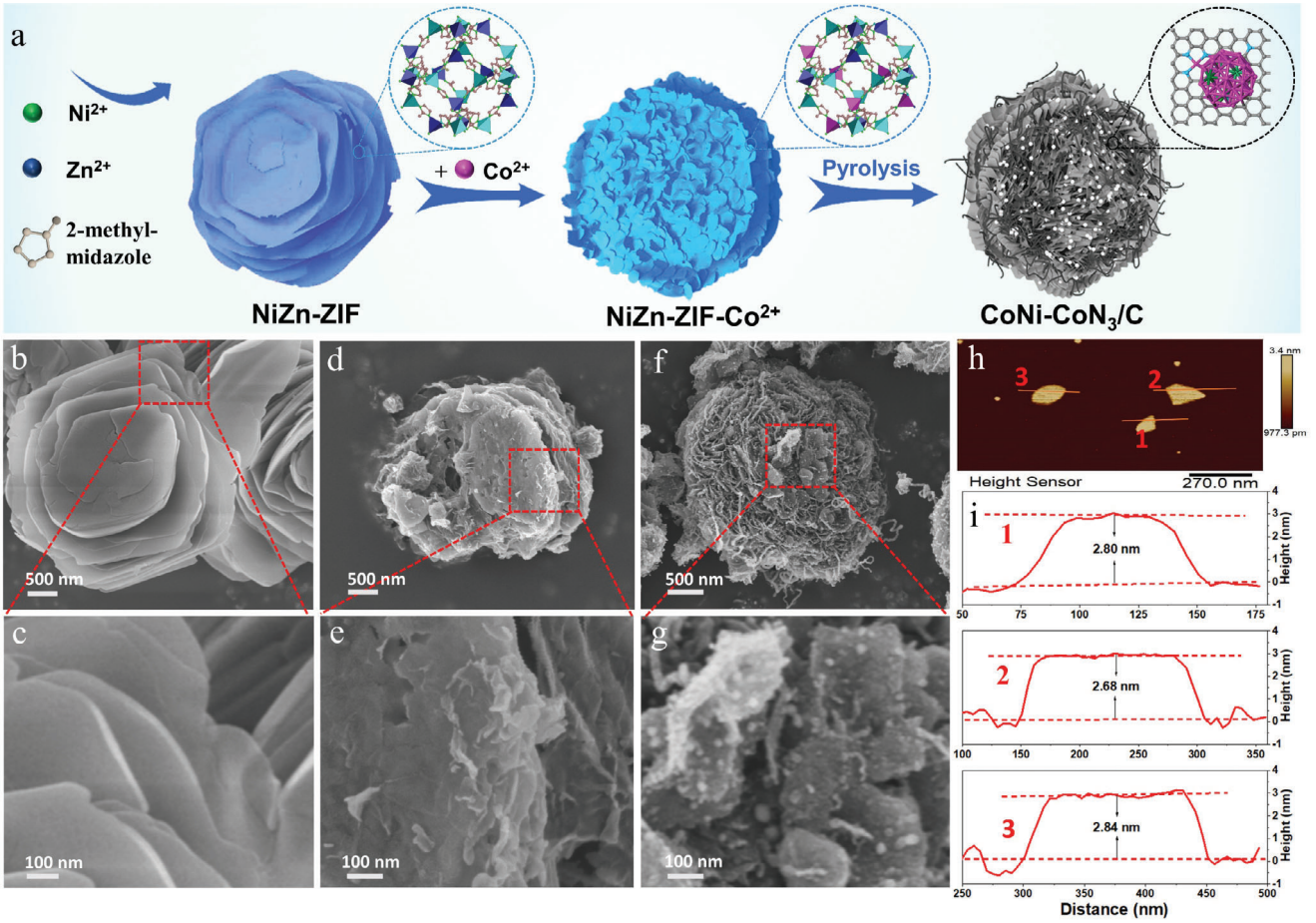

Figure 1. a) The synthesis route of CoNi-CoN_3/C. SEM images of (b,c) NiZn-ZIF, (d,e) NiZn-ZIF-Co^{2+}, and (f,g) CoNi-CoN_3/C. h,i) AFM image and height profiles of three different CoNi-CoN_3/C nanosheets.

XPS was used to characterize the chemical composition and bonding configuration of catalysts. The XPS survey spectrum reveals the presence of C, N, O, Co, and Ni in CoNi-CoN_3/C (**Figure** 3a). The corresponding atomic percent of the above elements is summarized in Table S1 (Supporting Information). Further analysis of high-resolution spectra leads to the following observations: 1) The C 1s XPS spectrum (Figure 3b) resolves three components at 284.8 (C—C═C), 285.8 (C—N), and 290.4 eV (C═O).[6] 2) The N 1s spectrum can be divided into five nitrogen configurations (Figure 3c), including pyridinic N (398.4 eV), pyrrolic N (399.3 eV), N—M (M = Co/Ni, 400.7 eV), graphitic N (401.7 eV) and oxidized N (405.7 eV).[39–41] 3) As for the O 1s spectrum (Figure S4a, Supporting Information), the peaks at 531.0, 532.2, and 533.5 eV are ascribed to C═O, nonlattice oxide at the surface (O_{sur}), and H—O, respectively.[35] 4) Only a weak Ni signal is detected due to the low content of Ni in samples (Figure S4b, Supporting Information). 5) High-resolution Co 2p spectrum in Figure 3d reveals the presence of Co (778.4 eV), Co—O (780.1 eV) and Co—N (781.9 eV) in CoNi-CoN_3/C.[42] The existence of Co—O signal in CoNi-CoN_3/C may originate from the surface oxidation of CoNi alloy in air, which is consistent with EDS results. In comparison with Co—N/C sample, the positions of Co—N peaks of CoNi-CoN_3/C shift towards lower energy, while Co and Co—O peaks shift towards higher energy, suggesting the existence of a strong electronic interaction between CoNi alloy and CoN_x moieties. Such strong interaction between CoNi alloyed NPs and CoN_x moieties may induce charge density redistribution around CoN_x sites, and thus optimizing the adsorption/desorption behaviors of key intermediates on active sites to promote the ORR and OER reactions.[43–45]

Synchrotron-based X-ray absorption fine structure (XAFS) spectroscopy was further performed to identify the local chemical environments of metal atoms in CoNi-CoN_3/C. **Figure** 4a displays the Co K-edge X-ray absorption near-edge structure (XANES) spectra of CoNi-CoN_3/C and reference samples including Co foil, CoO, Co_3O_4, and CoPc. The adsorption edge of CoNi-CoN_3/C is situated between those of Co foil and Co_3O_4, demonstrating that the valance state of Co species in CoNi-CoN_3/C is between zero-valent (Co^0) and oxidized $Co^{+8/3}$; and the result is consistent with the XPS analysis. Unlike the Co element, the Ni species in CoNi-CoN_3/C are basically in the form of zero-valent (Ni^0), which is verified by the Ni K-edge XANES spectrum (Figure 4b) and the corresponding fitting results (Figure S5, Supporting Information). To analyze the detailed coordination of Co and Ni species in CoNi-CoN_3/C, the Fourier transforms of extended X-ray absorption fine structure (FT-EXAFS) spectra at Co

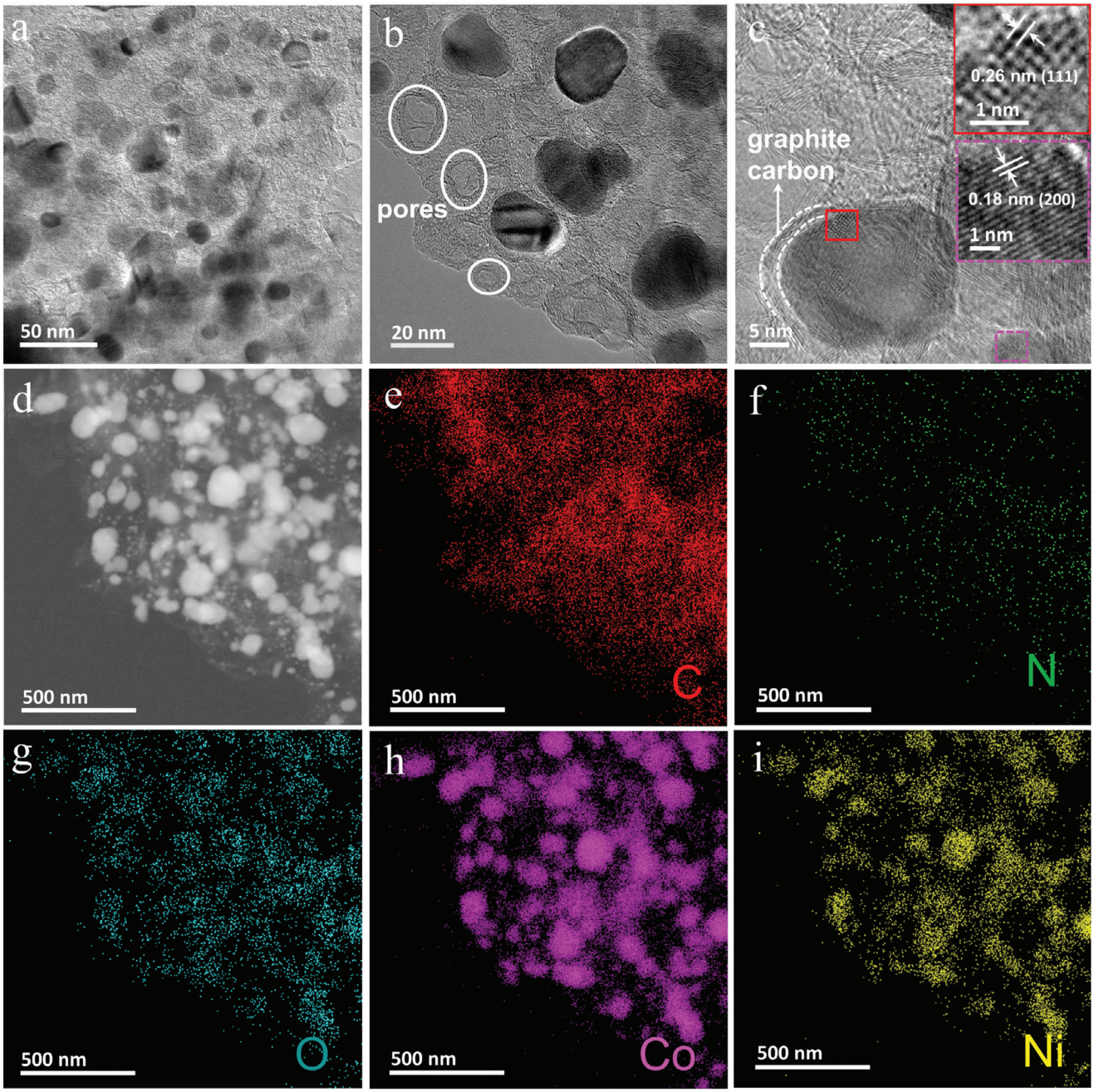

Figure 2. a) TEM images. b,c) high-resolution TEM image, and d–i) TEM and EDS elemental mapping images of CoNi-CoN_3/C.

and Ni K-edge are also provided, as presented in Figure 4c,d, respectively. The main peaks for the Co-K edge at ≈1.43 and 2.11 Å are assigned to Co—N and Co—Co/Ni, respectively; and the main peak for Ni—K edge at 2.16 Å is ascribed to Ni—Ni/Co coordination. Based on the fitting results of the EXAFS spectrum at the Co K-edge of CoNi-CoN_3/C (Figure 4e,f; Table S2, Supporting Information), the coordination number of Co atoms is ≈3, demonstrating the formation of approximate CoN_3 coordination. In addition, CoN_3, as the active center, has an asymmetric electron distribution and is more prone to four-electron ORR reaction than CoN_4, so it can be expected that the MN_x ($x = 3$) will have a positive effect on the ORR performance of the synthesized CoNi-CoN_3/C catalyst.[46] Moreover, as compared with those of Co and Ni foil (i.e., 12), smaller coordination numbers of the neighbor Ni—Ni/Co and Co—Co/Ni shells are calculated to be 7.9 ± 0.2 and 4.8 ± 0.2 in CoNi-CoN_3/C, respectively, signifying the partial Co and Ni species in CoNi-CoN_3/C exist in the form of alloy nanoparticles. There are interactions between different metal phases in CoNi alloys, which may synergistically improve the catalytic performance of OER. From the above analysis, it is concluded that the CoNi-CoN_3 composite sites (comprising CoNi alloyed NPs and CoN_3 moieties) are successfully created in the N-doped

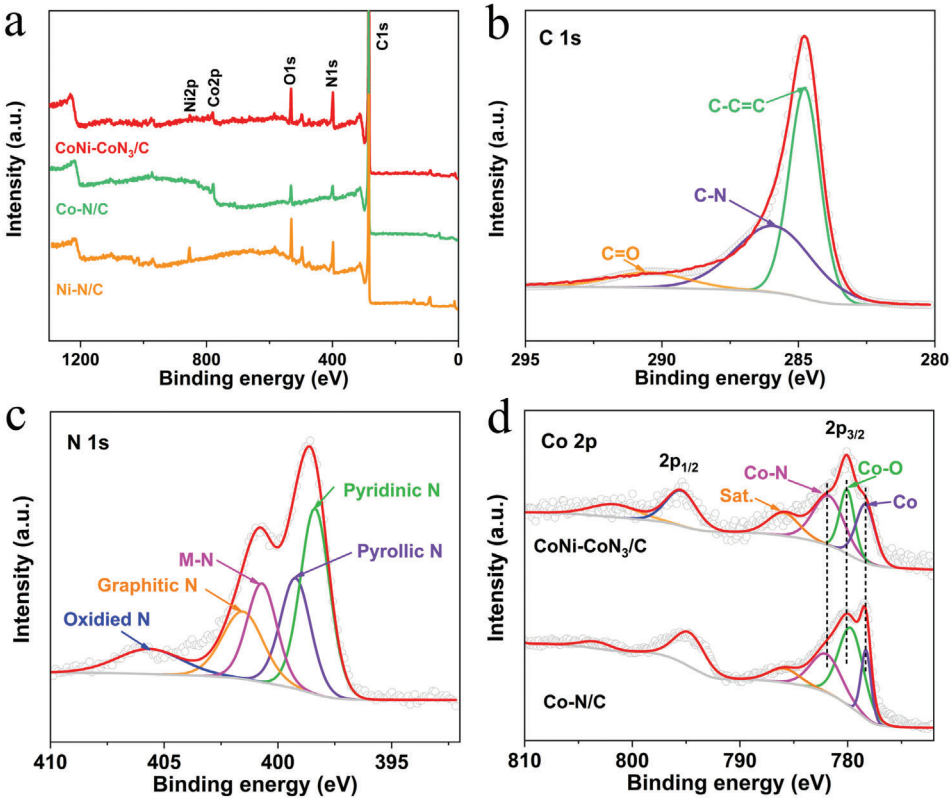

Figure 3. a) XPS survey spectra of CoNi-CoN_3/C, Co–N/C and Ni–N/C. High resolution b) C 1s and c) N 1s spectrum of CoNi-CoN_3/C. d) High resolution Co 2p spectra of CoNi-CoN_3/C and Co–N/C.

ultrathin carbon nanosheet matrix. In comparison with CoN_3 sites, the constructed CoNi-CoN_3 composite sites with modulated electronic structures are expected to synergistically accelerate the kinetic of ORR and OER.

2.2. ORR and OER Performance of CoNi-CoN_3/C

The ORR activity of catalysts was assessed in O_2-saturated 0.1 M KOH solution. As depicted in **Figure** 5a, a half-wave potential ($E_{1/2}$) of 0.88 V is acquired for CoNi-CoN_3/C, which is more positive than those of Pt/C (0.85 V), Co–N/C (0.81 V) and Ni—N/C (0.73 V), representing a superior ORR activity of CoNi-CoN_3/C. Remarkably, the ORR activity of CoNi-CoN_3/C also surpasses that of most recently reported M—N—C catalysts (Table S3, Supporting Information). The ORR kinetics were also evaluated based on the Tafel slope values calculated from the corresponding linear sweep voltammetry (LSV) curves. In comparison with Pt/C (93.9 mV dec^{-1}) and the control samples, the smallest Tafel slope of 74.0 mV dec^{-1} is obtained for CoNi-CoN_3/C (Figure 5b), revealing a favorable ORR kinetics.[47] As a result, CoNi-CoN_3/C delivers a kinetic current density (J_k) of 31.8 mA cm^{-2} at 0.85 V, which is ≈3.5 times larger than that of Co—N/C (i.e., 8.96 mA cm^{-2}), as summarized in Table S4 (Supporting Information). Figure 5c illustrates that the hydrogen peroxide yield of CoNi-CoN_3/C is below 10.7% over the potential range of 0.45–0.88 V (versus RHE), revealing a high ORR selectivity. The electron transfer number (n) of CoNi-CoN_3/C is calculated to be ≈4, revealing an efficient $4e^-$ transfer mechanism. Moreover, the linear and almost parallel Koutecky–Levich (K–L) curve of catayst reveal a first-order reaction kinetics for the dissolved O_2 (Figure S6, Supporting Information).[35] The stability of catalysts was investigated by using a current–time (i-t) chronoamperometric test. As depicted in Figure 5d, the CoNi-CoN_3/C exhibits outstanding stability with a high current retention of 92.9% after 10 h continuous test, in a sharp contrast to a large current loss of 35.1% of Pt/C within only 8 h under the same condition. The nearly unchanged ORR polarization curves before and after stability test demonstrate an outstanding performance reproducibility of CoNi-CoN_3/C catalyst (the inset in Figure 5d). The superb stability of CoNi-CoN_3/C can be also verified by its almost constant value of $E_{1/2}$ after cyclic voltammetry (CV) tests for 20 000 cycles (Figure S7, Supporting Information). The high ORR stability of CoNi-CoN_3/C is ascribed to its well-preserved CoNi-CoN_3 composite sites and hierarchical micro/mesoporous structure after the long-term stability test, as verified by the SEM and XPS measurements (Figure S8, Supporting Information). Moreover, CoNi-CoN_3/C also possesses excellent methanol tolerance, suggesting its potential application in direct methanol fuel cells (Figure S9, Supporting Information).

The OER performance of the as-prepared catalysts was also evaluated in 0.1 M KOH solution. A lower potential of 1.59 V than those of Co—N/C (1.61 V) and Ni—N/C (1.68 V), is obtained at 10 mA cm^{-2} ($E_{j=10}$) for CoNi-CoN_3/C, suggesting that the CoNi-CoN_3/C has a higher activity for catalyzing OER

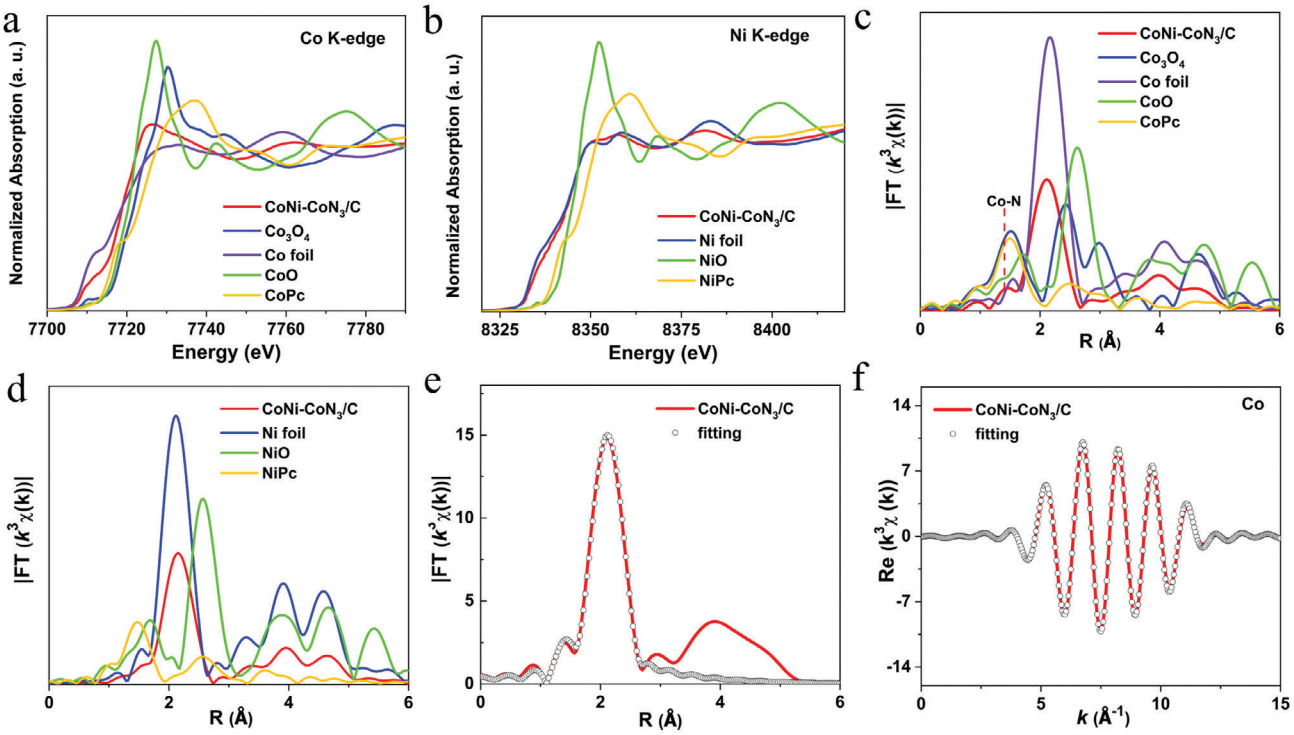

Figure 4. a) Co and b) Ni K-edge XANES spectra. Fourier transformed (FT) k^3-weighted $\chi(k)$-function of EXAFS spectra of c) Co and d) Ni elements in CoNi-CoN_3/C. e,f) EXAFS fitting curves of Co element in CoNi-CoN_3/C at R and k space. The data for Co K-edge of references (Co foil, CoO, Co_3O_4, CoPc) are from Ref. [35].

(Figure 5e). Additionally, the overpotential of the CoNi-CoN_3/C sample is lower than that of Ir/C at a large current density, e.g., 90 mA cm^{-2}. And the result is further supported by the kinetics analysis where CoNi-CoN_3/C shows the smallest Tafel slope value (134.7 mV dec^{-1}) among all tested samples, as presented in Figure 5f. Notably, the OER performance of CoNi-CoN_3/C is comparable to some recently reported M—N—C catalysts summarized in Table S5 (Supporting Information). Moreover, the double layer capacitances (C_{dl}) of CoNi-CoN_3/C and control samples were obtained based on CV tests at various scan rates (Figure S10, Supporting Information), and thus to evaluate their specific catalytic activity. In comparison with the control samples of Co—N/C (30.79 mF cm^{-2}) and Ni—N/C (19.70 mF cm^{-2}), CoNi-CoN_3/C has the largest C_{dl} value of 51.73 mF cm^{-2} (Figure 5g), agreeing its lowest potential for catalyzing OER. The outstanding OER durability of CoNi-CoN_3/C is confirmed by its high relative current density (94.3%) and nearly unchanged $E_{j=10}$ value (5 mV), as indicated by the *i*–t chronoamperometric response curves (Figure 5h) and CV curves after 20 000 cycles (Figure S11, Supporting Information), respectively. The high OER stability of CoNi-CoN_3/C attributed to its well-preserved structure of metal alloy nanoparticles supported on porous nanosheets during the stability test, as demonstrated by the SEM and XPS measurements (Figure S12, Supporting Information). The encapsulation of highly active CoNi-CoN_3 composite sites in the multi-layered graphite shells with rich micropores is believed to be able to prevent degeneration and corrosion of CoNi-CoN_3, and thereafter result in a high stability of CoNi-CoN_3/C. In addition, the reversible potential difference (ΔE) is the main reference for determining the excellent grade of bifunctional electrocatalytic activity of oxygen electrodes. As presented in Figure 5i and Table S6 (Supporting Information), the ΔE value of CoNi-CoN_3/C is 0.71 V, which is smaller than those of commercial Pt/C+Ir/C couple (0.72 V) and the control samples (Co—N/C and Ni—N/C), and suggests better overall activities and reversibility of CoNi-CoN_3/C electrode.[48] Additionally, a series of CoNi-CoN_3/C catalysts with different Co content were synthesized by adjusting the concentration of Co^{2+} in precursor mixed solution. Electrochemical measurements revealed that the appropriate Co content in CoNi-CoN_3/C catalysts has a significant impact on enhancing the ORR activity, while it has little effect on the OER activity (Figures S13 and S14, Supporting Information). Therefore, the precise control of Co content is of great significance for the synthesis of CoNi-CoN_3/C catalysts with optimal overall activity.

2.3. Electrocatalytic Mechanism

To reveal the interactions between CoNi alloy and CoN_3 moiety as well as the influences on the electrochemical performances, we have carried out DFT calculations regarding the electronic structures and thermodynamic trends for the CoNi-CoN_3 structures.[49] First of all, the change of electronic distribution induced by the neighboring CoNi alloys in CoNi-CoN_3 is demonstrated (**Figure 6a**). The evident orbital coupling is noticed between CoNi alloy and CoN_3 moiety, which represents the strong interactions, further leading to the significant modulations of the electronic distributions near CoN_3 moiety. The electronic

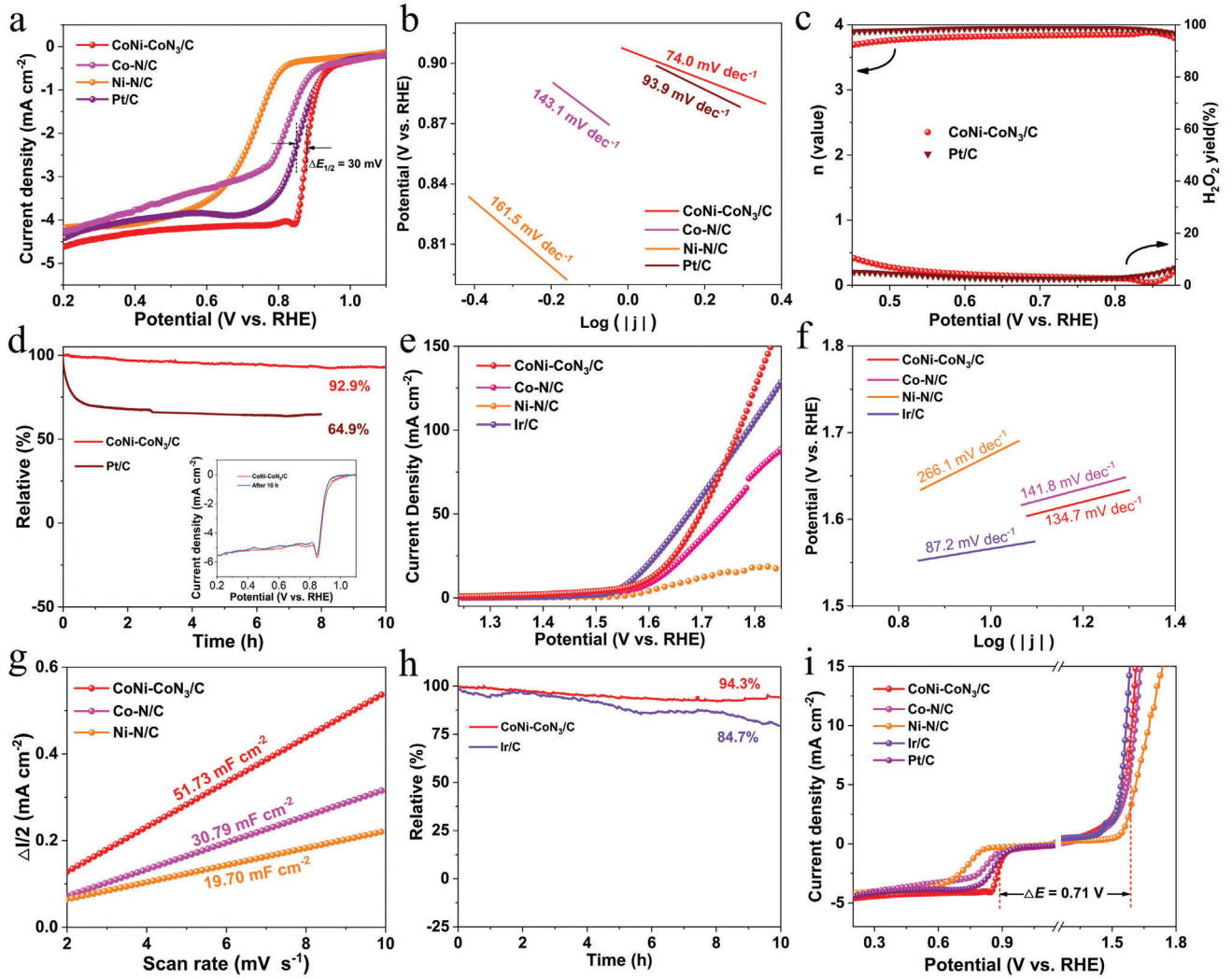

Figure 5. a) ORR polarization curves and b) the derived Tafel plots of CoNi-CoN_3/C and reference samples. c) H_2O_2 yield, electron transfer number and d) amperometric *i–t* curve of CoNi-CoN_3/C and Pt/C. The inset in (d) shows the LSV curves before and after ORR stability tests. e) OER polarization curves, and f) the derived Tafel plots of CoNi-CoN_3/C and reference samples. g) The calculated C_{dl} values of CoNi-CoN_3/C, Co—N/C, and Ni—N/C. h) Amperometric *i--t* curves of CoNi-CoN_3/C and Ir/C. i) The overall ORR and OER polarization curves of CoNi-CoN_3/C and reference samples.

redistribution near the active sites optimizes the stabilization of the key intermediates.[50] Notably, the bonding orbitals in CoNi-CoN_3 are dominated by both CoN_3 moiety and the surface Co sites in CoNi alloy, which are mainly distributed near the pristine CoN_3 moiety within a limited range (Figure 6b). Meanwhile, it is noted that the nearby substrate sites in CoN_3 are mostly constructed by the antibonding orbitals, limiting the site-to-site electron transfer within the substrate and decreasing the electronic conductivity.[51] The electronic structures are further analyzed by the projected partial density of states (PDOSs) to indicate the detailed contributions of different elements. For CoNi-CoN_3, it is noticed that the Co-3d orbitals in CoNi alloy and CoN_3 moiety are highly different (Figure 6c). Co-3d orbitals in the CoN_3 moiety exhibit a sharp peak near the Fermi level (E_F), playing as the main active sites for both ORR and OER. In comparison, the Co-3d orbitals in CoNi alloy are broadened and downshifted, which becomes more electron-rich and pins the Co-3d orbitals in CoN_3 moiety. Accordingly, the CoNi alloy acts as the electron reservoir to maintain the robust valence states of Co single atom sites in CoN_3 moiety during electrocatalysis.[52] For the CoNi-CoN_3 with surface oxidation on CoNi NPs (CoNi(oxi)–CoN_3), is revealed that the surface oxidation does not significantly affect the overall electronic structures of CoNi-CoN_3 (Figure S15a,b, Supporting Information). In comparison with the unoxidized structure, the dominant peak of Co-3d orbitals exhibits a converse trend in CoN_3 moiety and CoNi NPs, with a slight downshift and upshift, respectively. This observation supports the results from XPS characterization. The Co-3d orbitals in the pristine CoN_3 moiety are located in a slightly closer position to the E_F, compared to Co-3d orbitals in CoNi-CoN_3. This confirms the electronic modulations induced by the interactions between CoNi alloy and CoN_3 moiety (Figure 6d). However, the higher d-band center of Co sites potentially results in the over-binding issues of key intermediates, which cannot guarantee remarkable performance for both

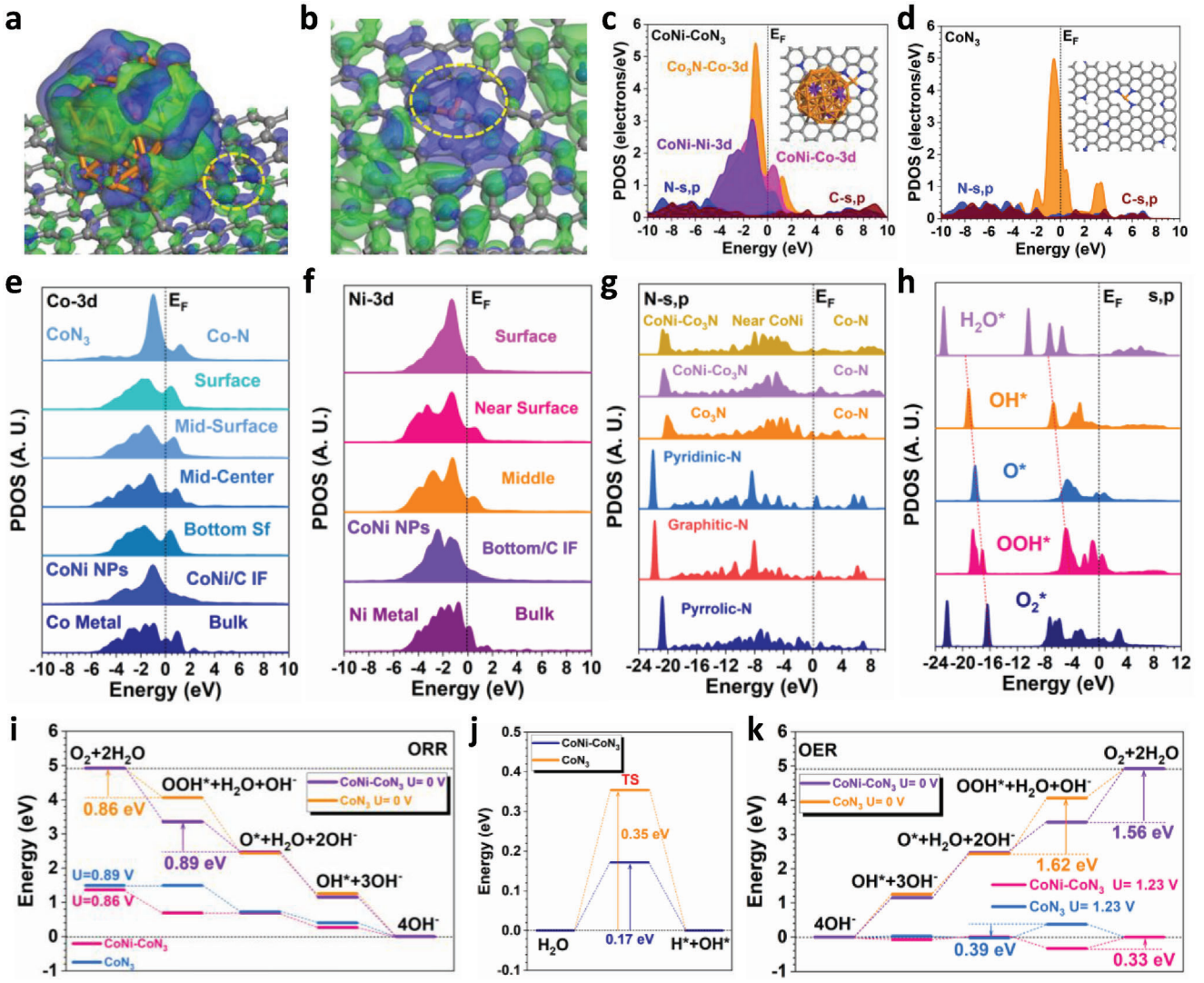

Figure 6. The electronic distributions of bonding and antibonding orbitals near the Fermi level of a) CoNi-CoN_3 and b) CoN_3. Yellow circles indicate the CoN_3 moiety. Orange balls = Co, Purple balls = Ni, Blue balls = N, Grey balls = C, and white balls = H. Blue isosurface = bonding orbitals and green isosurface = antibonding orbitals. The PDOSs of c) CoNi-CoN_3 and d) CoN_3. Insets are the relaxed structures of CoNi-CoN_3 and CoN_3. Site-dependent PDOSs of e) Co-3d and f) Ni-3d orbitals in CoNi-CoN_3. g) Site-dependent PDOSs of N in CoNi-CoN_3 and CoN_3. h) The PDOSs evolutions of key intermediates during ORR and OER. i) The reaction energy of ORR under $U = 0$ V and the applied potential. j) The energy barrier for water dissociation. k) The reaction energy of OER under $U = 0$ V and the equilibrium potential.

ORR and OER. Furthermore, the evolution of d-band center in different catalyst systems were further analyzed (Figure S15c,d, Supporting Information). In comparison with the pristine CoN_3 structure, the d-band center of the CoN_3 moiety in both CoNi-CoN_3 and CoNi(oxi)–CoN_3 is slightly downshifted (Figure S16c, Supporting Information), consistent with the XPS results indicating the electron transfer from CoNi NPs to Co^0 in CoN_3. We have also compared the d-band of metals in CoNi NPs and the overall d-band center (Figure S15d, Supporting Information). The d-band center of Co-3d orbitals in the oxidized CoNi NPs is slightly higher than that of the CoNi NPs, supporting an increase in valence states. Additionally, the d-band center of Ni remains stable, while the overall d-band centers of CoNi-CoN_3 and CoNi(oxi)-CoN_3 are much lower than that of CoN_3. The lower d-band center is crucial for optimizing the adsorption strengths of key intermediates in both ORR and OER processes.

A more in-depth analysis of the electronic structures is performed based on the site-dependent projected density of states (PDOSs). For Co-3d orbitals, the difference between CoNi alloy and CoN_3 moiety are clearly distinguished, where the Co sites in CoNi alloy are close to the metallic Co (Figure 6e). It is worth mentioning that the interfacial Co sites of CoNi display a sharp peak near the E_F, which improves the electron transfer between CoNi alloy and the substrate to improve the site-to-site electron transfer.[52] These results prove that there are two types of electronic structures for Co sites, where Co-3d in CoNi are able to optimize the electronic structures of Co-3d in CoN_3 for superior performances in both oxidation and reduction processes.

As displayed in Figure 6f, the Ni-3d orbitals in CoNi alloys are also close to the metallic Ni, indicating that most Ni sites show zero valence states as XAS characterized (Figure 4b,d). The surface Ni-3d orbitals in the alloy become sharp near the E_F, which overlaps with the Co-3d orbitals in the CoN_3 moiety to accelerate the site-to-site electron transfer between CoNi and CoN_3 moiety. The electronic structures of the N sites are also further investigated (Figure 6g). The s, p orbitals show a gradual downshifting trend from pyrrolic N sites to pyridinic N sites. The graphitic N exhibits the highest electron density near the E_F to support the electron transfer within the substrate. In contrast, the s, p orbitals of N sites in the CoN_3 moiety have upshifted due to the interactions with Co single atoms. The appearance of the neighboring CoNi alloys also increases the electron density near the E_F, which enhances the electron transfer within the electrocatalyst.[53] To evaluate the electron transfer efficiency during the intermediate conversion of ORR/OER, the PDOSs of the key intermediates are demonstrated (Figure 6h). Notably, the s, p orbital positions of intermediate display a relatively good linear relationship from O_2* to OH*, reducing the energy barriers of electron transfer for each step.[54] It is noted that the s, p orbitals of OOH* slightly deviate from the linear relationship, resulting in the potential rate-determining step (RDS) for both OER and ORR.

To explore the performances of both ORR and OER, the reaction energies of these two processes are further revealed to compare the reaction trends (Figure 6i). During the ORR process, the reaction energies exhibit a downhill trend, where the smallest energy change determines the RDS. The CoNi-CoN_3 has the RDS for the conversion from OOH* to O* while the RDS for CoN_3 is O_2 to OOH*, revealing the adsorption of OOH* is critical for the ORR performance as the analysis of electronic structures. Based on the RDS, CoNi-CoN_3, and CoN_3 require the applied potential of 0.89 and 0.86 V, respectively, to initiate the ORR without any energy barriers, indicating the superior performances of CoNi-CoN_3. For the water dissociation process, the CoNi-CoN_3 are able to facilitate the breaking of the O—H bond by the introduction of CoNi alloys, promoting the OER in the alkaline environment (Figure 6j).[55] The energy barrier of water dissociation in CoNi-CoN_3 is 0.17 eV, which is much smaller than that in CoN_3 (0.35 eV). Meanwhile, as the opposite reaction to ORR, the OER process shows continuously increasing reaction energies for both CoNi-CoN_3 and CoN_3 without any applied potential (Figure 6k). The RDS with the largest energy barrier is the OOH*→O_2 (1.56 eV) for CoNi-CoN_3, which is smaller than the RDS of CoN_3 at the conversion from O*→OOH* (1.62 eV). After applying the equilibrium potential of 1.23 V, the overpotentials of OER are estimated to be 0.33 and 0.39 V for CoNi-CoN_3 and CoN_3, respectively, supporting the enhanced performances of CoNi-CoN_3. Therefore, both electronic structures and reaction energies have confirmed the improved performances of CoNi-CoN_3 for both ORR and OER.

2.4. Performance of CoNi-CoN_3/C Based ZABs

Based on its preeminent bifunctional ORR/OER activity, aqueous rechargeable ZABs were assembled using CoNi-CoN_3/C as the catalyst in the oxygen electrode. As described in **Figure 7**a,b, the CoNi-CoN_3/C based aqueous ZABs deliver a high open circuit potential (OCP) of 1.57 V and a peak power density of 250 mW cm^{-2}, which are superior to those of Pt/C + RuO_2 based ZABs (1.41 V, and 127 mW cm^{-2}) and Pt/C + Ir/C based ZABs (1.43 V, and 100 mW cm^{-2}), highlighting the excellent battery performance. In addition, CoNi-CoN_3/C based aqueous ZABs also have advantages over some recently reported M—N—C catalyst based ZABs (Table S7, Supporting Information). The specific capacity of aqueous ZABs based on CoNi-CoN_3/C is 799 mAh g^{-1}, which are superior to those of Pt/C + Ir/C based ZABs (767 mAh g^{-1}) (Figure S16, Supporting Information). Moreover, a small voltage gap of 0.94 V is achieved for CoNi-CoN_3/C based battery; and it almost remains unchanged after continuous operation for 950 h (2850 charging/discharging cycles), demonstrating prominent cycling stability and reversibility of CoNi-CoN_3/C (Figure 7c). The morphology, structure, and chemical composition of CoNi-CoN_3/C after the cycling test were further investigated. It is revealed that the 2D nanosheet architecture of CoNi-CoN_3/C is well maintained (Figure S17, Supporting Information). The binding energy position and shape of the N 1s and Co 2p spectra of CoNi-CoN_3/C after cyclic testing are similar to those of freshly prepared samples, indicating that the structure of CoNi-CoN_3 composite active site is stable (Figure S18, Supporting Information). At the initial charging/discharging cycle, the coulomb efficiency of CoNi-CoN_3/C-based ZAB is calculated to be 66.9% at the current density of 20 mA cm^{-2} (Figure S19, Supporting Information). After 20 h continuous operation, the coulomb efficiency of battery is slightly reduced by 5.6%.

Furthermore, flexible and quasi-solid-state rechargeable ZABs were also assembled using CoNi-CoN_3/C as cathode (Figure 7d). The battery delivers a steady OCP of 1.43 V (Figure 7e), which is higher than that of the flexible battery based on Pt/C + Ir/C (1.41 V). The peak power density of CoNi-CoN_3/C based flexible ZAB was calculated to be 113 mW cm^{-2} (Figure 7f), which is comparable to and even better than that of the flexible battery based on Pt/C + Ir/C (88 mW cm^{-2}) and the recently reported flexible ZABs based on M—N—C catalysts (Table S8, Supporting Information). In particular, a high specific capacity of 804 mAh g^{-1} is achieved for CoNi-CoN_3/C based flexible ZAB (Figure 7g), which is higher than that of the flexible ZAB based on Pt/C + Ir/C (757 mAh g^{-1}) and in close proximity to the theoretical capacity (820 mAh g^{-1}) of ZABs. This suggests the highly efficient electrocatalytic performance of CoNi-CoN_3/C in practical applications. Continuous galvanostatic charging–discharging measurements were carried out to assess the cycling stability and reversibility of the flexible ZAB. As displayed in Figure 7h, the device shows an initial voltage gap of 0.67 V, which is smaller than that of the Pt/C + Ir/C based battery (0.72 V). Only a slight increase of 0.23 V in voltage gap is observed after a continuous test of 48 h, whereas the battery based on Pt/C+Ir/C undergoes severe performance degradation after only ≈33 h. Additionally, no remarkable change in charging and discharging voltages is revealed when the battery is repeatedly folded up to 90° (Figure S20, Supporting Information). The high energy efficiency, excellent reversibility, and strong durability of the flexible ZABs demonstrate the applicability of CoNi-CoN_3/C catalyst in both aqueous and quasi-solid-state rechargeable ZABs.

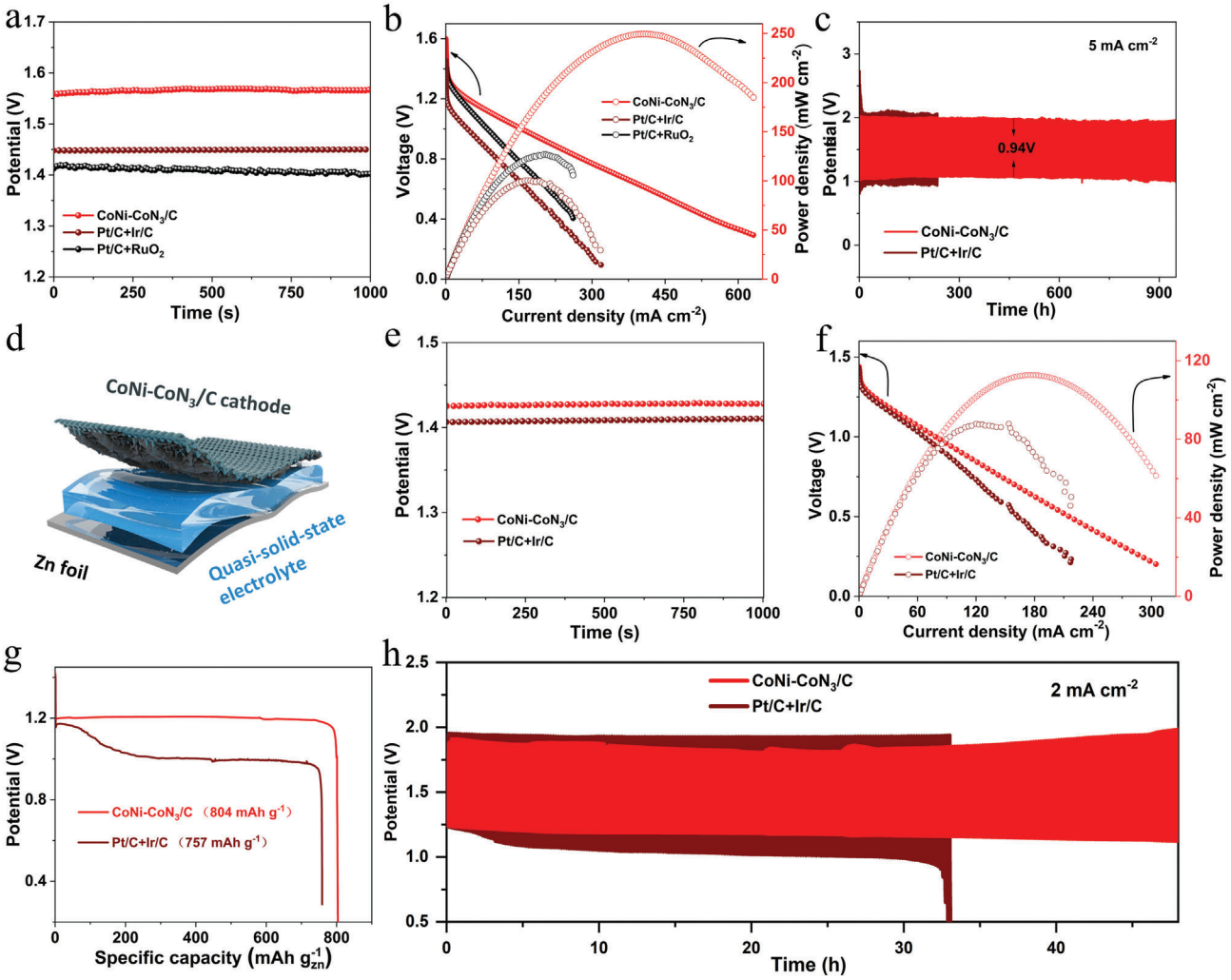

Figure 7. a) OCP curves, b) polarization curves and power density plots, and c) charging/discharging cycling curves at 5 mA cm^{-2} of aqueous ZABs based on various catalysts. d) Schematic diagram of the structure of CoNi-CoN_3/C-based flexible ZABs. e) OCP curves, f) polarization curves and power density plots, g) specific capacity, and h) charging/discharging cycling curves at 2 mA cm^{-2} of flexible ZABs based on CoNi-CoN_3/C and Pt/C+Ir/C.

According to the above results, we summarized the reasons for the excellent catalytic activity of CoNi-CoN_3/C catalyst:

1) Due to the asymmetric electronic state of three-coordinated CoN_3 moieties, the adsorption/desorption behaviors of the reaction intermediates are more easily regulated, resulting in abnormally high ORR activity of CoNi-CoN_3/C catalyst.
2) The adjacent CoNi alloys affected the electronic structure of CoN_3, resulting in a slight downward shift in the d-band center of the entire CoNi-CoN_3 composite sites, which improved the OER performance of CoNi-CoN_3 /C catalyst.
3) The strong interaction between CoNi alloy NPs and CoN_3 moieties regarding the modulations in electronic structures and reaction trends synergistically optimizes the ORR and OER reaction kinetics; 4) the large specific surface area and ultrathin nanosheet structure greatly improves the exposure and accessibility of the CoNi-CoN_3 composite sites, and fully releases the ORR and OER catalytic potential of CoNi-CoN_3/C catalyst.

3. Conclusion

In summary, novel CoNi-CoN_3 composite sites containing CoNi alloyed NPs and CoN_3 moieties have been constructed in N-doped porous carbon nanosheet matrix, and the composite sites show high catalytic activity towards both OER and ORR, i.e., a positive ORR half-wave potential of 0.88 V and a small OER overpotential of 360 mV at 10 mA cm^{-2} are achieved. Significantly, CoNi-CoN_3/C is applied as the catalyst of air electrodes in aqueous rechargeable ZABs, which exhibit a maximum power density of 250 mW cm^{-2} and superior durability of 950 h, and those of flexible quasi-solid-state ZABs are 113 mW cm^{-2} and 48 h, respectively. Such performances are highly competitive even when compared to those of most ZABs based on excellent M—N—C catalysts reported to date. Theoretical calculations have investigated the interactions between CoNi alloys and CoN_3 moiety regarding the modulations in electronic structures and reaction trends. The 3d orbitals of CoNi alloys not only optimize the Co-3d orbitals in CoN_3 moiety but also supply protection to achieve robust valence

states for high durability of active sites. The electronic modulations also realize the moderate adsorption of key intermediates, which ensures superior performance for both OER and ORR. The findings on understanding the catalytic mechanism of interactive M—NPs and MN_x moieties to guarantee remarkable performances of both OER and ORR provide a new approach for the design of efficient and bifunctional M—N—C catalysts for future battery applications.

Supporting Information

Supporting Information is available from the Wiley Online Library or from the author.

Acknowledgements

This study was supported by the National Natural Science Foundation of China (No. 52074119, 52172241, and 52304327), the National Key R&D Program of China (2021YFA1501101), the Joint Funds of National Natural Science Foundation of China (No. U20A20280), National Natural Science Foundation of China/Research Grant Council of Hong Kong Joint Research Scheme (N_PolyU502/21), the General Research Fund of Hong Kong (No. CityU 11308321), the Hunan Provincial Natural Science Foundation of China (No. 2022JJ30393 and 2023JJ40448), the Scientific Research Fund of Hunan Provincial Education Department (No. 22B0042), the Postgraduate Scientific Research Innovation Project of Hunan Province (No. CX20230517) and the Changsha Natural Science Foundation (No. kq2208160). The authors thank Shiyanjia Lab (www.shiyanjia.com) for the XPS characterization.

Conflict of Interest

The authors declare no conflict of interest.

Data Availability Statement

The data that support the findings of this study are available on request from the corresponding author. The data are not publicly available due to privacy or ethical restrictions.

Keywords

CoNi-CoN3 composite sites, oxygen evolution reaction, oxygen reduction reaction, synergistic electrocatalytic activity, zinc–air batteries

Received: February 26, 2024
Published online: March 3, 2024

[1] Z. Chen, X. Peng, Z. Chen, T. Li, R. Zou, G. Shi, Y. Huang, P. Cui, J. Yu, Y. Chen, X. Chi, K. P. Loh, Z. Liu, X. Li, L. Zhong, J. Lu, *Adv. Mater.* **2023**, *35*, 2209948.
[2] W. Li, L. Wu, X. Wu, C. Shi, Y. Li, L. Zhang, H. Mi, Q. Zhang, C. He, X. Ren, *Appl. Catal. B: Environ.* **2022**, *303*, 120849.
[3] N. Li, T. Yang, L. Huang, H. Jiang, J. Xiao, X. Ma, H. Lou, C. Xie, Y. Yang, *ACS Appl. Mater. Interfaces* **2023**, *15*, 52530.
[4] Y. Wang, K. Wang, J. Yu, Y. Ma, X. Yang, H. Jiang, Y. Liu, J. Li, W. Li, *J. Power Sources* **2021**, *482*, 228897.
[5] T. Yang, N. Li, D. Wei, C. Xie, Y. Yang, H. Jiang, *J. Electroanal. Chem.* **2023**, *941*, 117552.
[6] J. Li, W. Li, H. Mi, Y. Li, L. Deng, Q. Zhang, C. He, X. Ren, *J. Mater. Chem. A* **2021**, *9*, 22635.
[7] Y. Xue, Y. Guo, Q. Zhang, Z. Xie, J. Wei, Z. Zhou, *Nano-Micro Lett.* **2022**, *14*, 162.
[8] X. Xu, J. Xie, B. Liu, R. Wang, M. Liu, J. Zhang, J. Liu, Z. Cai, J. Zou, *Appl. Catal. B: Environ.* **2022**, *316*, 121687.
[9] H. Jiang, J. Gu, X. Zheng, M. Liu, X. Qiu, L. Wang, W. Li, Z. Chen, X. Ji, J. Li, *Energy Environ. Sci.* **2019**, *12*, 322.
[10] Y. Guan, N. Li, J. He, Y. Li, L. Zhang, Q. Zhang, X. Ren, C. He, L. Zheng, X. Sun, *J. Mater. Chem. A* **2021**, *9*, 21716.
[11] H. Zhang, S. Zuo, M. Qiu, S. Wang, Y. Zhang, J. Zhang, X. W. Lou, *Sci. Adv.* **2020**, *6*, eabb9823.
[12] M. Liu, Z. Lyu, Y. Zhang, R. Chen, M. Xie, Y. Xia, *Nano Lett.* **2021**, *21*, 2248.
[13] Y. Guan, N. Li, Y. Li, L. Sun, Y. Gao, Q. Zhang, C. He, J. Liu, X. Ren, *Nanoscale* **2020**, *12*, 14259.
[14] J. Yu, Y. Wang, L. Zhu, H. Jiang, J. Hao, Y. Zhang, M. Liu, J. Li, X. Ji, W. Li, *ACS Appl. Mater. Interfaces* **2019**, *11*, 45596.
[15] N. Li, T. Yang, H. Lou, L. Huang, X. Ma, H. Jiang, J. Xiao, C. Xie, Y. Yang, *Sustainable Energy Fuels* **2023**, *7*, 5240.
[16] H. Jiang, J. Xia, L. Jiao, X. Meng, P. Wang, C.-S. Lee, W. Zhang, *Appl. Catal. B: Environ.* **2022**, *310*, 121352.
[17] L. Yang, L. Shi, D. Wang, Y. Lv, D. Cao, *Nano Energy* **2018**, *50*, 691.
[18] K. Chen, S. Kim, M. Je, H. Choi, Z. Shi, N. Vladimir, K. H. Kim, O. L. Li, *Nano-Micro Lett.* **2021**, *13*, 60.
[19] Q. Zhang, J. Guan, *Adv. Funct. Mater.* **2020**, *30*, 2000768.
[20] M. Xiao, H. Zhang, Y. Chen, J. Zhu, L. Gao, Z. Jin, J. Ge, Z. Jiang, S. Chen, C. Liu, W. Xing, *Nano Energy* **2018**, *46*, 396.
[21] S. Lai, L. Xu, H. Liu, S. Chen, R. Cai, L. Zhang, W. Theis, J. Sun, D. Yang, X. Zhao, *J. Mater. Chem. A* **2019**, *7*, 21884.
[22] Y. Wang, X. Cui, L. Peng, L. Li, J. Qiao, H. Huang, J. Shi, *Adv. Mater.* **2021**, *33*, 2100997.
[23] P. Li, H. Wang, X. Tan, W. Hu, M. Huang, J. Shi, J. Chen, S. Liu, Z. Shi, Z. Li, *Appl. Catal. B: Environ.* **2022**, *316*, 121674.
[24] J. Liu, J. Xiao, B. Luo, E. Tian, G. I. N. Waterhouse, *Chem. Eng. J.* **2022**, *427*, 132038.
[25] Y. X. Zhao, J. H. Wen, P. Li, P. F. Zhang, S. N. Wang, D. C. Li, J. M. Dou, Y. W. Li, H. Y. Ma, L. Xu, *Angew. Chem., Int. Ed.* **2023**, *62*, e202216950.
[26] H. Meng, B. Wu, D. Zhang, X. Zhu, S. Luo, Y. You, K. Chen, J. Long, J. Zhu, L. Liu, S. Xi, T. Petit, D. Wang, X.-M. Zhang, Z. J. Xu, L. Mai, *Energy Environ. Sci.* **2024**, *17*, 704
[27] K. Ding, J. Hu, J. Luo, L. Zhao, W. Jin, Y. Liu, Z. Wu, G. Zou, H. Hou, X. Ji, *Adv. Funct. Mater.* **2022**, *32*, 2207331.
[28] X. Cheng, Y. Li, J. Zheng, S. Yin, C. Wang, X. Qu, J. Yang, Y. Jiang, S. Sun, *Nano Energy* **2022**, *100*, 107440.
[29] S.-H. Yin, J. Yang, Y. Han, G. Li, L.-Y. Wan, Y.-H. Chen, C. Chen, X.-M. Qu, Y.-X. Jiang, S.-G. Sun, *Angew. Chem., Int. Ed.* **2020**, *59*, 21976.
[30] X. Cheng, J. Yang, W. Yan, Y. Han, X. Qu, S. Yin, C. Chen, R. Ji, Y. Li, G. Li, G. Li, Y. Jiang, S. Sun, *Energy Environ. Sci.* **2021**, *14*, 5958.
[31] S. H. Yin, J. Yang, Y. Han, G. Li, L. Y. Wan, Y. H. Chen, C. Chen, X. M. Qu, Y. X. Jiang, S. G. Sun, *Angew. Chem., Int. Ed.* **2020**, *59*, 21976.
[32] J. Liu, C. Wang, H. Sun, H. Wang, F. Rong, L. He, Y. Lou, S. Zhang, Z. Zhang, M. Du, *Appl. Catal. B: Environ.* **2020**, *279*, 119407.
[33] R. He, T. Lu, N. Xu, G. Liu, Y. Zhang, J. Qiao, *Chem. Eng. J.* **2023**, *461*, 141843.
[34] W. Huang, C. Su, C. Zhu, T. Bo, S. Zuo, W. Zhou, Y. Ren, Y. Zhang, J. Zhang, M. Rueping, H. Zhang, *Angew. Chem., Int. Ed.* **2023**, *62*, e202304634.
[35] Y. Liu, Z. Chen, Z. Li, N. Zhao, Y. Xie, Y. Du, J. Xuan, D. Xiong, J. Zhou, L. Cai, Y. Yang, *Nano Energy* **2022**, *99*, 107325.
[36] Z. Chen, B. Fei, M. Hou, X. Yan, M. Chen, H. Qing, R. Wu, *Nano Energy* **2020**, *68*, 104371.

[37] J. Zhang, F. Tang, K. Wan, Y. Yang, C. Zhang, P. W. Ming, B. Li, *J. Mater. Chem. A* **2022**, *10*, 14866.
[38] N. Li, Y. Guan, Y. Li, H. Mi, L. Deng, L. Sun, Q. Zhang, C. He, X. Ren, *J. Mater. Chem. A* **2021**, *9*, 1143.
[39] A. Yang, K. Su, W. Lei, Y. Tang, X. Qiu, *Adv. Energy Mater.* **2022**, *13*, 2203150.
[40] H. Jiang, Y. Liu, W. Li, J. Li, *Small* **2018**, *14*, e1703739.
[41] A. I. Douka, Y. Xu, H. Yang, S. Zaman, Y. Yan, H. Liu, M. A. Salam, B. Y. Xia, *Adv. Mater.* **2020**, *32*, 2002170.
[42] J. Wang, Z. Huang, W. Liu, C. Chang, H. Tang, Z. Li, W. Chen, C. Jia, T. Yao, S. Wei, Y. Wu, Y. Li, *J. Am. Chem. Soc.* **2017**, *139*, 17281.
[43] X. Li, H. Wu, A. M. Elshahawy, L. Wang, S. J. Pennycook, C. Guan, J. Wang, *Adv. Funct. Mater.* **2018**, *28*, 1800036.
[44] Q. Liu, Z. Xue, B. Jia, Q. Liu, K. Liu, Y. Lin, M. Liu, Y. Li, G. Li, *Small* **2020**, *16*, e2002482.
[45] C. Zhao, L. Tian, Z. Zou, Z. Chen, H. Tang, Q. Liu, Z. Lin, X. Yang, *Appl. Catal. B: Environ.* **2020**, *268*, 118445.
[46] X. Sun, K. Li, C. Yin, Y. Wang, F. He, H. Tang, Z. Wu, *Phys. Chem. Chem. Phys.* **2017**, *19*, 17670.
[47] C. Hu, L. Dai, *Adv. Mater.* **2017**, *29*, 1604942.
[48] D. Chen, X. Chen, Z. Cui, G. Li, B. Han, Q. Zhang, J. Sui, H. Dong, J. Yu, L. Yu, L. Dong, *Chem. Eng. J.* **2020**, *399*, 125718.
[49] M. Z. Rahman, F. Raziq, H. Zhang, J. Gascon, *Angew. Chem., Int. Ed.* **2023**, *62*, e202305385.
[50] Z. Qiao, C. Wang, C. Li, Y. Zeng, S. Hwang, B. Li, S. Karakalos, J. Park, A. J. Kropf, E. C. Wegener, Q. Gong, H. Xu, G. Wang, D. J. Myers, J. Xie, J. S. Spendelow, G. Wu, *Energy Environ. Sci.* **2021**, *14*, 4948.
[51] K. Wang, Y. Wang, B. Yang, Z. Li, X. Qin, Q. Zhang, L. Lei, M. Qiu, G. Wu, Y. Hou, *Energy Environ. Sci.* **2022**, *15*, 2356.
[52] Y. Song, M. Sun, S. Zhang, X. Zhang, P. Yi, J. Liu, B. Huang, M. Huang, L. Zhang, *Adv. Funct. Mater.* **2023**, *33*, 2214081.
[53] X. Shen, H. Li, Y. Zhang, T. Ma, Q. Li, Q. Jiao, Y. Zhao, H. Li, C. Feng, *Appl. Catal. B: Environ.* **2022**, *319*, 121917.
[54] H. Li, Y. Han, H. Zhao, W. Qi, D. Zhang, Y. Yu, W. Cai, S. Li, J. Lai, B. Huang, L. Wang, *Nat. Commun.* **2020**, *11*, 5437.
[55] Z. Sun, L. Lin, J. He, D. Ding, T. Wang, J. Li, M. Li, Y. Liu, Y. Li, M. Yuan, B. Huang, H. Li, G. Sun, *J. Am. Chem. Soc.* **2022**, *144*, 8204.